Aeroacoustic Investigation of a Propeller Operating at Low Reynolds Numbers

Grande, Edoardo; Romani, Gianluca; Ragni, Daniele; Avallone, Francesco; Casalino, Damiano

DOI
10.2514/1.J060611

Publication date
2022

Document Version
Final published version

Published in
AIAA Journal

AIAA JOURNAL
Vol. 60, No. 2, February 2022

Aeroacoustic Investigation of a Propeller Operating at Low Reynolds Numbers

Edoardo Grande,* Gianluca Romani,† Daniele Ragni,‡ Francesco Avallone,§ and Damiano Casalino¶
Delft University of Technology, Delft, 2629HS, The Netherlands

https://doi.org/10.2514/1.J060611

This paper presents an experimental investigation of a propeller operating at low Reynolds numbers and provides insights into the role of aerodynamic flow features on both propeller performances and noise generation. A propeller operating at a tip Reynolds number regime of $4.3 \times 10^4 - 4.38 \times 10^4$ is tested in an anechoic wind tunnel at an advance ratio ranging from 0 to 0.6. Noise is measured by means of a microphone array, while aerodynamic forces are measured with load and torque cells. Oil-flow visualizations are used to show the flow patterns on the blade surface, whereas phase-locked stereoscopic particle image velocimetry (PIV) measurements are carried out to analyze the flow at 60% of the blade radius. The pressure field around the blade section has been computed from the PIV velocity data. Results reveal a complex flowfield with the appearance of a laminar separation bubble at the suction side of the blade. The separation bubble moves toward the leading edge and reduces in size as the advance ratio decreases. At an advance ratio equal to 0.6, the flowfield is characterized by a laminar separation without reattachment. This causes vortex shedding responsible for a high-frequency hump in the far-field noise spectra.

Nomenclature

a, a'	=	tangential and radial induction coefficients
B	=	number of propeller blades
C_p	=	pressure coefficient
C_Q	=	torque coefficient
C_T	=	thrust coefficient
c	=	blade chord, m
D	=	propeller diameter, m
f	=	frequency, Hz
J	=	advance ratio
n	=	propeller rotational speed, Hz
p	=	air static pressure, Pa
Q	=	torque, Nm
Re_c	=	chord-based Reynolds number
Re_{60}	=	Reynolds number based on the chord at the 60% of the blade span
T	=	thrust, N
V_R	=	flow velocity in the relative (rotating) frame, m/s
V_{rms}	=	rms of relative velocity, m/s
V_T	=	blade tangential velocity, m/s
V_∞	=	freestream velocity, m/s
ρ	=	air density, kg/m^3
ω	=	propeller rotational speed, rpm
ω_z	=	spanwise vorticity component, s^{-1}

Subscripts

R	=	rotating reference frame
∞	=	freestream condition

Received 4 February 2021; revision received 28 June 2021; accepted for publication 5 August 2021; published online 21 September 2021.

*Ph.D. Candidate, Aerodynamics, Wind Energy, Flight Performance and Propulsion Department; e.grande@tudelft.nl. Member AIAA.
†Ph.D. Candidate, Aerodynamics, Wind Energy, Flight Performance and Propulsion Department; g.romani@tudelft.nl. Member AIAA.
‡Associate Professor, Aerodynamics, Wind Energy, Flight Performance and Propulsion Department; d.ragni@tudelft.nl. Member AIAA.
§Assistant Professor, Aerodynamics, Wind Energy, Flight Performance and Propulsion Department; f.avallone@tudelft.nl. Member AIAA.
¶Professor, Aerodynamics, Wind Energy, Flight Performance and Propulsion Department; d.casalino@tudelft.nl. Member AIAA.

I. Introduction

THE interest in the aeroacoustics of rotors operating at a chord Reynolds number Re_c ranging from 10^4 to 10^5 has considerably increased in the last few years due to the fast development of unmanned aerial vehicles (UAVs), micro air vehicles, and personal air vehicles. Unmanned vehicles applications span across military and civilian fields, including delivery of goods, real-time monitoring, mapping, aerial imaging, surveillance, infrastructure inspection, and many others.

Currently, the most employed propulsive system for these types of vehicles consists of propellers, since they offer the thrust-to-weight ratio to hover and to perform quick maneuvers in close vicinity of an obstacle. The fast expansion of the drones market will be closely related to rotor noise abatement. The acoustic impact of a PAV hovering over an urban area and undertaking an approach maneuver over flat terrain has been recently addressed by Casalino et al. [1,2]. Another disadvantage of multirotor UAVs is constituted by the limited flight time (around 20–30 min), directly related to the propellers' aerodynamic performance, which deteriorates at Reynolds numbers below 10^5.

Several studies focusing on airfoils at low Reynolds numbers ($Re_c < 5 \cdot 10^5$) prove that they exhibit a very high sensitivity of the performance to the Reynolds number itself and a complicated boundary-layer physics including laminar separation, transition, and reattachment [3–6]. For this reason, the design and optimization of propellers operating at low Reynolds numbers are currently limited. The work of Serre at al. [7] addresses the issue of designing a quiet and efficient propeller by developing a numerical tool containing an aerodynamic model based on Xfoil, an acoustic model. A reduction of 10 dB is observed between the conventional rotor and the optimized one. Even though the final result is satisfactory, the authors show the limitations of using a viscous–inviscid method like Xfoil as an aerodynamic solver for such low Reynolds numbers. Comparisons with experiments show that the airfoil (NACA0012) drag coefficient is underestimated by nearly 30% over a range of angles of attack going from 0 deg to 30 deg, and the lift coefficient is overestimated up to a maximum of about 40%. Moreover, the boundary-layer thickness, which is one of the input parameters of the broadband noise model, exhibits a different trend with respect to the experimental one. The experimental works of Brendel and Mueller [8] and Kim et al. [9] on airfoils at a maximum $Re_c = 2 \cdot 10^5$ show that the integral boundary-layer parameters are strongly influenced by the presence of a laminar separation bubble. The displacement thickness increases rapidly after a laminar separation and decreases at transition onset, whereas the momentum thickness exhibits a sudden increase

near the transition location. These behaviors are usually not captured by low-fidelity methods.

The boundary layer on airfoils at low Reynolds numbers and moderate angles of attack is usually subjected to a laminar separation; however, the separated shear layer quickly undergoes turbulent transition and reattaches on the airfoil surface, forming a laminar separation bubble (LSB). The size and location of the LSB depends on the angle of attack, Reynolds number, and airfoil geometry. As the angle of attack (or Reynolds number) increases, the LSB moves toward the leading edge and decreases in length [10] until it bursts at the leading edge, causing a sudden decrease in lift and increase in drag. In this case, a laminar separation is present, but the free shear layer is not able to reattach immediately. This condition is typically referred to as "long bubble". When the Reynolds number decreases, the LSB bursts at low angles of attack, negatively affecting the lift curve slope. The angle of attack at which an LSB bursts in this "long" form is strongly dependent on the Reynolds number and airfoil geometry. Bastedo and Mueller [11] studied the flow characteristics over a Wortmann FX63-137 airfoil at $Re_c = 8 \cdot 10^4$ and $2 \cdot 10^5$. In the first case, the LSB bursts for angles of attack less than 6 deg, whereas for $\alpha > 6$ deg a short bubble is formed, increasing lift and decreasing drag. In the second case, an LSB is present from $\alpha = -7$ deg to 21 deg, where it bursts. Park et al. [12] show that the flow over a DAE51 airfoil at $Re_c = 3.9 \cdot 10^4$ does not reattach up to $\alpha = 10$ deg. The study of Yarusevych et al. [13] shows a similar trend for an NACA0025 airfoil: at $\alpha = 5$ deg and $Re_c = 5.5 \cdot 10^4$, a boundary-layer separation without reattachment is observed; when the Reynolds is increased to 10^5, an LSB is formed. Coherent structures generated from the separated shear layer [9,14,15] can result in vortex shedding noise, as will be explained later.

The low-Reynolds number aerodynamic characteristics illustrated in the previous section are expected to have also an influence on noise generation. Studies focusing on small-scale propellers' aeroacoustics [16,17] show that the noise spectra exhibit both a tonal contribution, generated by the periodic blade loading and by the periodic displacement of fluid due to the finite thickness of the blade [18], and a broadband contribution. For the latter, the main noise sources are turbulent boundary-layer trailing-edge noise and turbulent ingestion noise at the leading edge. Beside these typical noise sources, it is still not clear if phenomena characteristic of low-Reynolds number flows, such as LSB, can represent an important noise source for propellers. Studies on steady airfoils prove that the vortex shedding from an LSB can generate tonal or quasi-tonal noise. The experimental work of Pröbsting and Yarusevych [19] on an NACA0012 airfoil shows that the passage of the vortices generated from an LSB over the trailing edge produces tonal noise. A necessary condition for the noise emission is that these structures are generated sufficiently close to the trailing edge and retain enough coherence. As a result, the acoustic pressure waves scattered at the trailing edge propagate upstream and force the amplified shear-layer disturbances. On the other side, the work of Wu et al. [20] associates the near-wake shedding, originated from an LSB on an airfoil at low Reynolds, with a high frequency hump in the far-field noise spectra.

Passive methods for noise reduction of small propellers are also of great interest. Yang et al. [21] adopted a different design of sawtooth trailing-edge serration on a UAV propeller. A broadband noise reduction is observed for all the serrated models, up to a maximum of 8 dB. Lee et al. [22] conducted experimental testing on rotors with flat-tip trailing-edge serration, that is, the sawtooth serration where the sharp tip is cut in order to become flat, and rectangular serrations. The flat-tip serrated propeller showed the highest broadband noise attenuation at 3000 rpm, corresponding to an overall noise reduction of 5.8 dBA. The main mechanism for noise reduction of serrated propellers is associated to destructive scattering efficiency.

The goal of the paper is to study the flow around the blade of a propeller operating at low Reynolds numbers and to evaluate if the flow is attached/separated, if a laminar-to-turbulent transition is present, and if an LSB is formed. The knowledge about the flow behavior is then linked to the global aerodynamic performance and the noise generation. In particular, an attempt to shed more light on the contribution of low-Reynolds phenomena on the noise emission is given. To this purpose, surface oil-flow visualizations and phase-locked stereoscopic PIV of a cross-sectional plane of the blade have been performed for the propeller operating at an advance ratio ranging between 0 and 0.6. The characteristics of the boundary layer are retrieved from the analysis of the oil-flow patterns, rms velocity, spanwise vorticity distribution, and static pressure, calculated from the PIV velocity. Far-field noise measurements have been performed through a linear array of microphones. For each condition, thrust and torque time signals have also been acquired by means of load and torque cells. In addition, the experimental challenges faced in order to get accurate measurements, such as the uncertainty due to variations of rotational speed and motor noise contamination, are described.

The paper is organized as follows. In Sec. II the propeller geometry, the experimental setup, and the experimental test matrix are presented. In Sec. III the experimental uncertainties are illustrated. Finally, in Sec. IV the characteristics of the flow around the blade, the aerodynamic performances, and the noise emitted are discussed.

II. Experimental Setup and Procedures

The experiments have been carried out in the anechoic tunnel (A-tunnel) at the low-speed laboratory of TU Delft. The A-tunnel is a vertical, open-jet wind tunnel, where the surrounding of the nozzle exit consists of an anechoic chamber with the walls covered by melamine wedges. A circular exit nozzle with a diameter of 0.60 m and a contraction ratio of 15 : 1 has been employed for this study. The maximum flow speed that the A-tunnel is able to provide with this nozzle is 35 m/s, the mean streamwise velocity is uniform whithin 0.6% of freestream velocity, and the turbulence intensity is 0.14% at 2.5 m/s and decreases below 0.1% with a flow velocity above 10 m/s. A description of the tunnel, with details of the flow and acoustic characterizations, can be found in the paper of Merino-Martinez et al. [23].

A. Propeller Design

The propeller used for this study has been obtained from an APC 9×6, diameter of 9″ (22.86 cm) and pitch of 6″ (15.24 cm), a model aircraft two-bladed propeller that routinely operates at a low Reynolds number. The diameter has been scaled up to $D = 30$ cm and each profile has been reshaped with an NACA 4412 airfoil. An elliptical section at the root has been merged with the first profile section starting from a radius of 1 cm (Fig. 1a). An in-house tool, made by a combination of Matlab and SolidWorks software, has been employed for the blade design. The chord and twist angle distributions of the blade over the radial distance r from the hub center are shown in Fig. 1b. The maximum chord is $c_{\max} = 3.4$ cm and the maximum twist angle is $\beta_{\max} = 43.6$ deg.

The propeller, made of aluminium alloys, has been manufactured using computer numerical control machining at TU-Delft with 0.4 to 0.8 μm Ra finish. This manufacturing method guarantees high accuracy and minimizes the surface imperfections, which can induce vibrations during the measurements and can affect the quality of the flow around the blades.

B. Propeller Test Rig

The test rig, mounted in the A-tunnel, is shown in Fig. 2a. The propeller is connected to a profiled aluminium nacelle of 5 cm diameter for minimum interference with the propeller flow. Within the nacelle, a motor, an encoder, a load cell, and a torque cell are assembled. The nacelle is supported by stiffened hollow aluminum NACA 0012 profiles of 6 cm chord, inside which all the cablings are housed and remotely connected to the instrumentation outside the jet. The entire structure is held up above the nozzle of the tunnel by four steel-wire tubes of 2 cm diameter fixed to the tunnel to minimize vibrations and interference. The different parts of the rotor drivetrain are shown in Fig. 2b with different colors: in yellow, the encoder disk; in red, the motor; in gold, the torque cell; in violet, a load cell; and in gray, connectors.

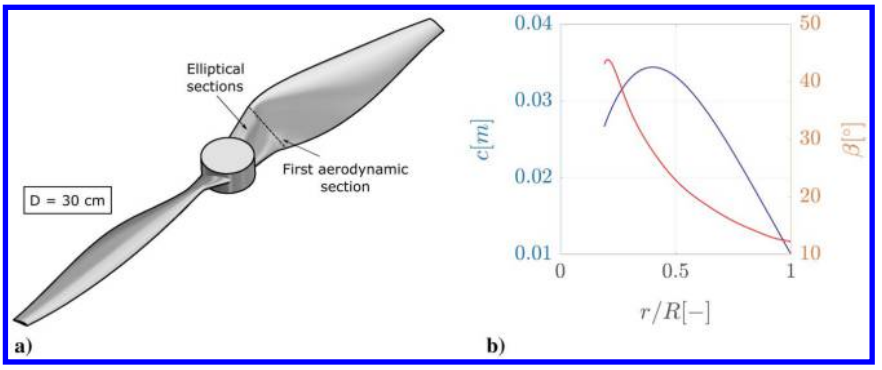

Fig. 1 a) Propeller CAD geometry and b) blade chord and pitch angle distributions.

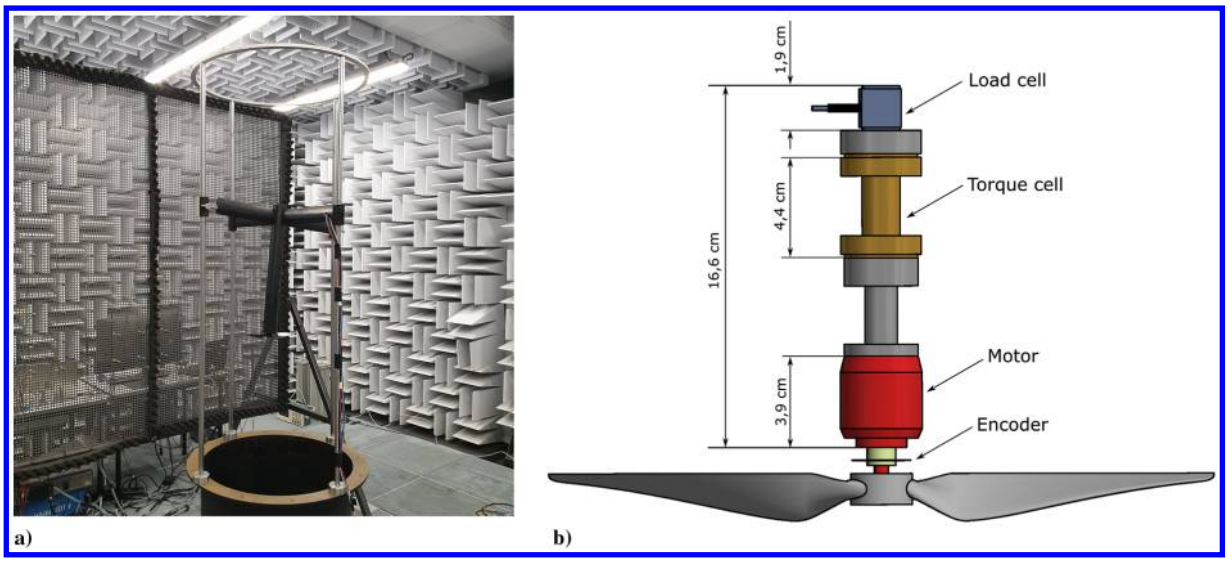

Fig. 2 a) Propeller setup mounted in the A-tunnel at TU-Delft and b) propeller drive train from bottom to top: yellow, the encoder disk; red, the motor; gray, a connector; gold, the torque cell; n gray, a second connector; and violet, a load cell.

The propeller is driven by an electrical brushless motor, Leopard Hobby 3536-5T 1520 KV, with a diameter of 27.8 mm and maximum power of 550 W. The motor is powered by a Delta Elektronika DC power supply with a voltage range of 0–15 V and a current range of 0–100 A. The motor rotational speed is measured by means of a US Digital EM1 transmissive optical encoder, coupled with a US Digital disk of 25.4 mm diameter and 200 cycles per revolution (1.8 deg of uncertainty on the position).

Rotor thrust is measured using a uniaxial Futek LSB200 load cell excited with 5 volts of direct current (VDC). The load cell is characterized by a maximum capacity of 22.2 N, nonlinearity and histeresis of $\pm 0.1\%$ of rated output (RO), and an operating temperature between -50 and 90°C. The torque is measured using a Transducer Techniques RTS-25 torque sensor excited with 10 VDC. It has a maximum capacity of 0.18 Nm, nonlinearity and histeresis of $\pm 0.1\%$ of RO, and an operating temperature between -54 and 93°C. The thrust and torque signals are acquired by a National Instrument acquisition board with a sampling frequency of 5 KHz and an acquisition time of 15 s. Thrust and torque coefficients and propulsive efficiency are calculated using the following definitions:

$$C_T = \frac{T}{\rho n^2 D^4} \qquad C_Q = \frac{Q}{\rho n^2 D^5} \qquad \eta_{\text{prop}} = \frac{C_T J}{2\pi C_Q} \tag{1}$$

where T is the thrust in N, Q the torque in Nm, ρ the air density in kg/m^3, n the propeller rotational frequency in Hz, D the propeller diameter in m, and $J = V_\infty / nD$ the advance ratio, being V_∞ the axial flow speed in m/s.

C. Acoustic Measurements Apparatus

A planar microphone array, sketched in Fig. 3, located in a plane perpendicular to the propeller plane, has been used. The array is constituted by 13 G.R.A.S. 40PH analog free-field microphones, having a diameter of 7 mm, a frequency range between 10 and 20 KHz, and a maximum sound pressure level (SPL) of 135 dB. The microphones have been calibrated using a G.R.A.S. 42AA pistonphone with a calibration level of 114 dB (reference sound pressure of 20 μPa). The uncertainty of the calibration is less than 0.09 dB (99% confidence level). The data acquisition system consists of a National Instrument PXIe-4499 sound and vibrations data acquisition module. As Fig. 3 shows, the array is at 4D (1.2 m) in the y direction with respect to the propeller axis. The distance between each microphone is 0.5D (0.15 m), the microphone 7 is at the propeller plane, the microphone 1 is 3D (0.9 m) above the propeller plane, and the microphone 13 is 3D below. Microphone voltages have been recorded for a duration of 30 s at a frequency rate of 50 KHz. The acoustic signals are separated in 300 Welch blocks with 50% overlap, corresponding to a bandwidth of 10 Hz.

D. PIV Measurements Apparatus

Stereoscopic PIV measurements have been conducted to study the flow over the cross section of the blade at $r/R = 60\%$ ($c = 3$ cm). The stereoscopic PIV setup is shown in Fig. 4a. The flow is seeded with particles of 1 micrometer median diameter produced by a SAFEX Twin Fog generator with SAFEX-Inside-Nebelfluid, a mixture of dyethelene glycol and water. The particles are introduced in the wind tunnel circuit to ensure a uniform concentration while recirculating in the test section. Illumination of the field of view is provided by a double cavity Quantel Evergreen EVG00200 Nd:YAG

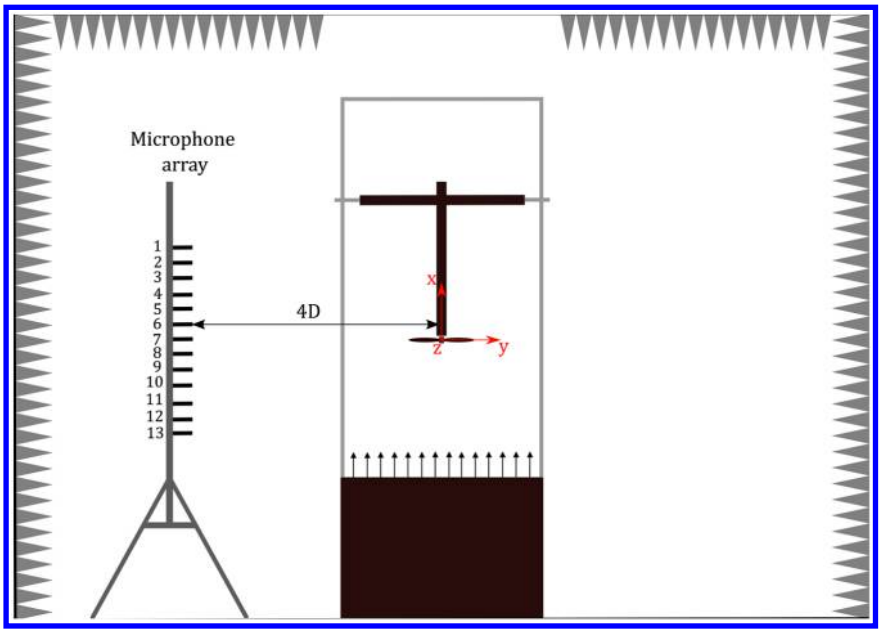

Fig. 3 Microphone array configuration.

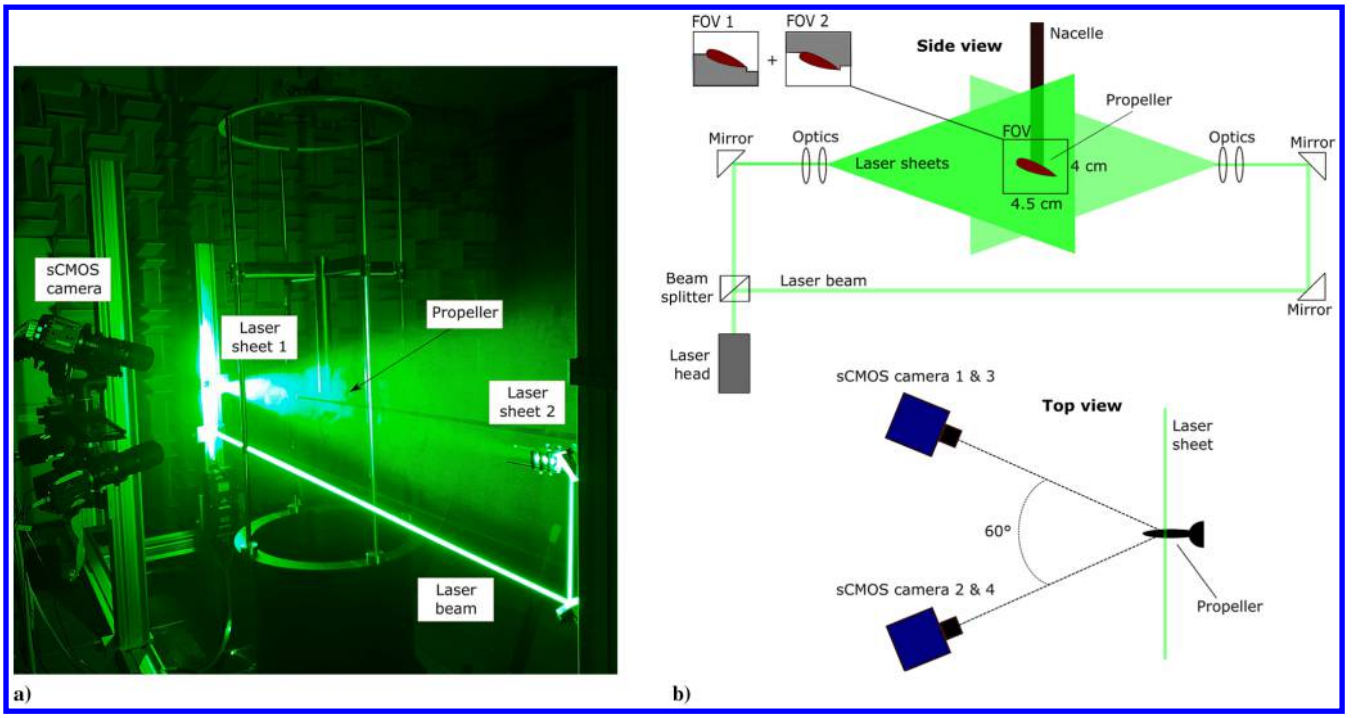

Fig. 4 a) Picture of the stereoscopic PIV setup and b) sketch of PIV laser and camera configurations.

laser with 200 mJ/pulse energy. To measure the flow over a cross section of the airfoil, two laser sheets of about 1 mm have been created, one illuminating the suction side of the airfoil and one the pressure side, in order to avoid shadow regions in the field of view. The latter has been obtained as a combination of two fields of view, as shown in Fig. 4b. The white area shown in the schematic represents the part combined for the full field-of-view visualization. Figure 4b shows also the laser and camera configurations. Four Imager sCMOS camera (two for the suction side and two for the pressure side) with 2560×2160 pixels and four Nikon lenses with 200 mm focal length at f# 11 have been used for the cross-section measurements. In order to focus on the measurement plane, Scheimpflug adapters have been mounted on each camera. Sets of 500 images have been recorded in phase-locked mode. To obtain phase-locked measurements, a trigger signal from the encoder mounted on the motor shaft has been used to control the timing of laser and camera. By specifying a trigger delay in the software, the images have been acquired when the propeller section is aligned with the laser plane, as depicted in Fig. 4b (bottom). The camera calibration, acquisition, and postprocessing have been carried out with LaVision Davis 8.4 software. The images are processed with a window deformation iterative multigrid [24] with a final interrogation window size of 24×24 pixels and 75% overlap. Spurious vectors are isolated through a median filter and replaced by interpolation. Details of the PIV setup apparatus are collected in Table 1.

E. Flow Analysis and Pressure Computation

Following the approach of Ragni et al. [25], the flow around the blade has been evaluated with respect to a noninertial reference frame, that is, a reference frame that is rotating at the propeller rotational speed ω. This means that the rotational velocity component

Table 1 Details of PIV setup

Imaging parameters		PIV processing	
Camera	4 Imager sCMOS	Software	LaVision Davis 8.4
Number of pixels, px	2560 × 2160	Pulse separation, μs	10
Pixel size, μm	6.5 × 6.5	Number of recordings	500
Focal length, mm	200	Minimum window size, px^2	24 × 24
Magnification	0.37		
Imaging resolution, px/mm	≈56		
FOV, cm^2	≈4.5 × 4		
Spatial resolution, mm	≈ > 0.4		
f#	11		

of the blade section $\boldsymbol{V}_T = \boldsymbol{\omega} \times \boldsymbol{r}$ (with $\boldsymbol{r}$ being the position vector) has been subtracted from the x component of the PIV velocity fields. Indeed, since the blade section chord is small compared to the propeller radius, $\boldsymbol{V}_T$ can be approximated to a translational motion aligned with the x component of the flow velocity.

Assuming that no thermal energy is added, the total temperature in the relative frame is constant, and the PIV velocity data can be used to compute the pressure field p around the blade section [26]. This indirectly gives information about the boundary-layer characteristics.

The pressure has been retrieved by integration of the pressure gradient as obtained from the Navier–Stokes momentum equations (under incompressible flow conditions) with velocity input from PIV, neglecting the Reynolds turbulent stresses, which were found to give a negligible contribution in the pressure computation:

$$\nabla \cdot (\nabla p) = \nabla^2 p = -\rho \nabla \cdot (\boldsymbol{V}_R \cdot \nabla)\boldsymbol{V}_R \tag{2}$$

The integration has been carried out by combining the pressure gradient via a Poisson equation and validated through a finite marching algorithm as in Oudheusden [26]. As boundary conditions, the pressure has been prescribed on the boundaries where the flow can be considered isentropic (Dirichlet boundary conditions), and the pressure gradient has been imposed on the remaining boundaries (Neumann conditions). The very last extrapolation on the airfoil geometry is carried out by using the gradient on the first point with finite differences. The blade section at 60% radius has been chosen as one of the most representative outboard profiles, where the out-of-plane gradients are negligible with respect to the in-plane one. In the vicinity of the blade, in fact, the in-plane spatial velocity derivatives are of the order of 10^4 s^{-1}, compared to prospected changes of out-of-plane velocity v_z component of the order of 10^2 s^{-1} (assuming that v_z doubles in a spanwise strip length equal to $R/10$). Therefore, the in-plane pressure can be reconstructed on the airfoil with sufficient accuracy. Once the pressure is integrated, the pressure coefficient can be calculated as follows:

$$c_P = \frac{p - p_\infty}{0.5\rho_\infty V_{R\infty}^2} \tag{3}$$

where the subscript∞ refers to freestream conditions.

F. Oil-Flow Visualization

Surface oil-flow visualization has been performed to visualize flow patterns on the propeller blade. The latter is sprayed with a fluorescent mixture, obtained from 50 mL liquid-paraffin wax and 15–25 drops of fluorescent oil additive A-680, in order to cover the propeller surface with a continuous film of oil. The propeller has been brought to the required operating conditions by combining the speed of the tunnel fan and of the propeller controller in order to have an almost constant thrust coefficient. Hence the propeller has been run for 8–10 min at constant operating conditions, allowing the paraffin to develop over the surface and reach the final configuration, and then slowly stopped. The propeller at rest has been illuminated by an ultraviolet lamp with a wide aperture, positioned perpendicular to the model, and images are obtained by acquiring snapshots of the blade surface at an angle of about 30 deg.

G. Experimental Test Matrix

The propeller has been operated both in hover and freestream flow conditions. Hence, the rotational speed has been kept constant at 4000 rpm to limit the variation of Reynolds number, and the advance ratio J has been varied. When J increases (freestream velocity V_∞ increases), the angle of attack over the blade decreases. This is evident from the drawing (see Fig. 5) of two velocity triangles for a generic blade section at the same tangential velocity and two different advance ratios $J_2 > J_1$, corresponding to $V_{\infty_2} > V_{\infty_1}$. In the figure, θ is the pitch angle, α is the angle of attack, $\phi = \theta - \alpha$ is the inflow angle, and a and a' are the tangential and radial induction coefficients. The experimental test matrix is summarized in Table 2. For each case the corresponding value of advance ratios J and Reynolds number Re_{60}, based on the chord at 60% of the span (which is the location chosen for the flow measurements), are indicated.

III. Experimental Uncertainty and Acoustic Contamination

A. RPM Variability in the Measurements

The first uncertainty that has been taken into account is the variation of the propeller rotational speed during the measurements. A variation of rpm causes a variation of the blade lift, which is directly associated to the loads and tonal noise emission. The rpm variation has been calculated from the encoder signal, acquired simultaneously with the load and noise measurements. The encoder signal is constituted by a one-per-revolution signal, and the rpm variation in time is retrieved from the time difference between two pulses. The hover condition exhibits the higher rpm variation, that is, ±20 rpm of deviation from the mean value; at $J = 0.12$ the variation is ±6 rpm, while the other advance ratios show an rpm variation between 2 and 4.

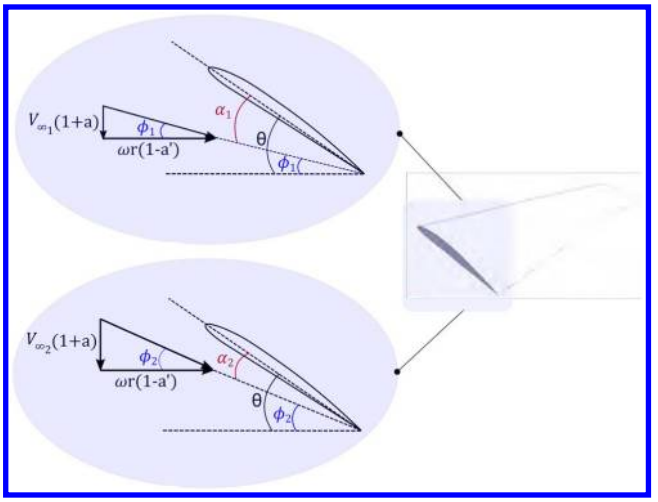

Fig. 5 Velocity triangles for a fixed-blade section at two different freestream velocities $V_{\infty_1} > V_{\infty_2}$.

Table 2 Experimental test matrix

Case	rpm	V_∞, m/s	J	Re_{60}
1	4000	0.0	0.0	$7.67 \cdot 10^4$
2	4000	2.4	0.12	$7.68 \cdot 10^4$
3	4000	4.8	0.24	$7.73 \cdot 10^4$
4	4000	8.0	0.4	$7.83 \cdot 10^4$
5	4000	12	0.6	$8.04 \cdot 10^4$

B. Loads and Noise Uncertainties

The uncertainty of thrust and torque have been computed from the scatter of the measurements on different days, and they have been found to be 0.1 and 0.05%, respectively. The uncertainty due to the variability of the propeller rotational speed is calculated by retrieving the thrust and torque values from chunks of signals of 10-revolutions' length and computing the standard deviation. The uncertainty found for the thrust measurements is equal to 4.8% at $J = 0$, 3.6% at $J = 0.12$, and between 0.6 and 1.1% for the other advance ratios. On the other side, the torque uncertainty is 0.1% at $J = 0$ and between 0.02 and 0.06% for the other advance ratios.

The signal from the encoder, acquired simultaneously with the noise measurements, has also been used to calculate the uncertainty of the blade passing frequency (BPF) 1 level associated to a variation of the propeller rotational speed during the measurements. Figure 6 (left) shows the pressure signals over time measured with microphone 7, at 4000 rpm and $J = 0.0$, 0.24, and 0.6 (from top to bottom) together with the encoder signals, whereas 6 (right) shows the propeller rpm variation in time. For clarity's sake, only 0.2 s out of 30 s of signals are shown. Following the same approach used for the load uncertainty, the pressure signals have been cut in chunks of 10 revolutions, and, for each of them, the first BPF tone SPL has been computed and the standard deviation evaluated. The results for each advance ratio and three microphones are reported in Table 3. The maximum uncertainty in hover is about 2 dB and is higher with respect to $J = 0.12$, 0.24, and 0.4 cases, because of the higher variation of rpm over time. The $J = 0.6$ case presents uncertainty values similar to the hover case; this is due to the low-frequency component in the pressure signal, clearly visible from Fig. 6 (bottom right). It is supposed that this effect is associated with the tunnel flow jet noise, whose contribution is not negligible at low frequencies with increasing flow velocity.

C. PIV Uncertainty

In the present stereoscopic experiment, a self-calibration through a disparity correction procedure is used [27], in order to refine the target calibration by correlation of the particle images between the two cameras. The residual average misalignment is equal to 0.03 pixels (px). The phase-locked PIV measurements of this study are mainly affected by random uncertainty, as the cross-correlation uncertainty. The effect of this error scales with $1/\sqrt{N}$ (where N is the number of images), due to statistical convergence. The cross-correlation uncertainty is expected to be in a range of 0.05–0.1 px [28], for a multipass algorithm ending with a window size of 24×24 px. The corresponding error based on the value of maximum instantaneous velocity, encountered at the airfoil suction side, is of the order of 0.9%, while the minimum velocity, encountered at the airfoil leading edge, is equal to 5%. Therefore, the overall uncertainty on the maximum and minimum mean velocities are assessed at 0.04 and 0.22%, respectively.

Table 3 First BPF tone level uncertainty at 4000 rpm due to variations of rotational speed

	Std, dB				
Mic	$J = 0.0$	$J = 0.12$	$J = 0.24$	$J = 0.4$	$J = 0.6$
1	2.13	1.54	0.65	1.37	2.38
7	1.08	0.94	0.42	0.88	1.89
13	1.34	0.87	0.44	1.05	2.06

On the other side, the overall uncertainty relative to the maximum and minimum velocity fluctuations are of the order of 1.7 and 14%, respectively. The uncertainty due to spatial resolution depends on the size λ of the structures to be resolved and on the interrogation window size ws, in this case equal to 0.4 mm. The vortical structures identified in the instantaneous images and localized in the airfoil wake have a dimension of 0.8 to 1.5 mm, creating a mean wake profile of about 2.5 mm thickness. The normalized window size of $ws/\lambda = 0.06$ can be converted into a spatial resolution error of <5% for such structures, as shown by Schrijer and Scarano [29].

D. Motor and Background Noise

In Fig. 7 the combined propeller/motor noise at 4000 rpm and three different advance ratios, $J = 0$, 0.24, and 0.6 (corresponding to $V_\infty = 0$, 4.8, 8 m/s), measured with microphone 7 of the array (see Fig. 3), has been compared with the motor noise without propeller and with the background noise of the facility. The frequency axis of each plot is normalized with respect to the the blade passing frequency BPF $= Bn$, where B is the number of blades and n is the propeller rotational frequency in Hz. The background noise (dashed black line) is comparable with the propeller broadband noise in the low-frequency range at $J = 0.6$ ($V_\infty = 8$ m/s). When the advance ratio is below 0.6, the signal-to-noise ratio is higher than 10 dB over almost the entire spectrum. The electrical motor noise (dashed light blue line) exhibits a series of discrete tones in the range BPF 5–BPF 100 (660 Hz–13 kHz) and a broadband level that does not affect the noise measurements, being more than 10 dB lower than the propeller noise over the entire frequency range for all the cases. The imperfect blade-loading balancing causes the rise of harmonics at BPF 0.5, 1.5, and 2.5. As a final remark, an additional source of tonal noise in the experiment is constituted by vibrations of test rig and rotor. The quantification of the latter is left for future experiments

IV. Aerodynamic and Aeroacoustic Characterization

A. Oil-Flow Visualization

Oil-flow visualizations of the suction side of the propeller blade at b) $J = 0.24$ ($V_\infty = 4.8$ m/s), c) $J = 0.4$ ($V_\infty = 8$ m/s), and

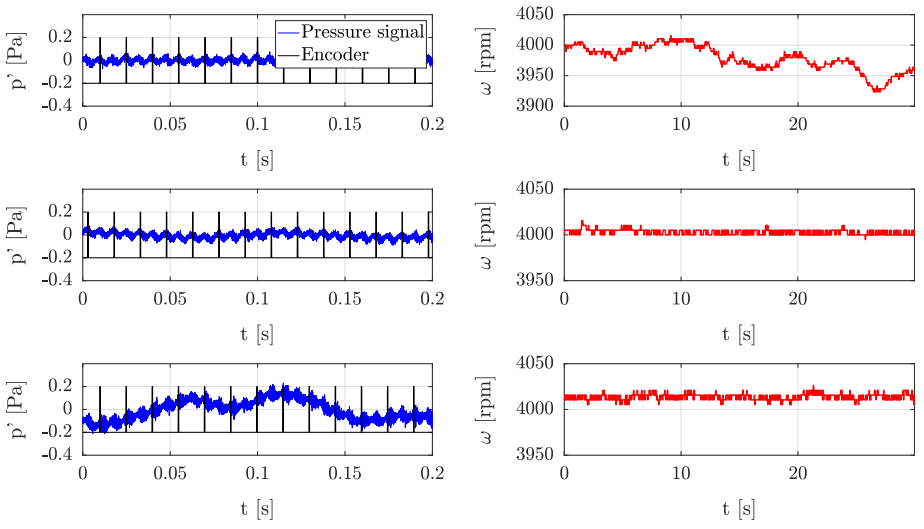

Fig. 6 Pressure and encoder signal (left) and velocity signal (right) over time at 4000 rpm and $J = 0.0$, 0.24, and 0.6 (from top to bottom).

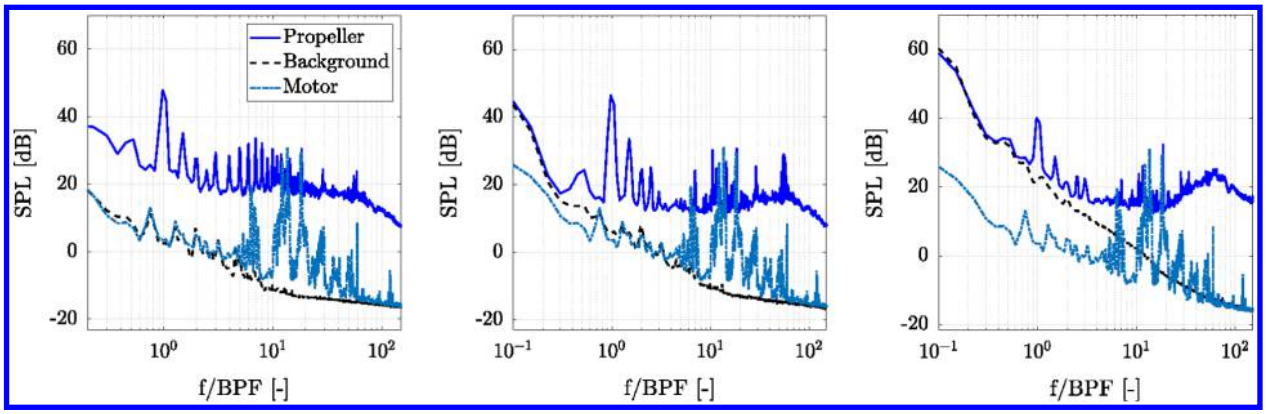

Fig. 7 Comparison between propeller noise and background/motor noise at 4000 rpm and $J = 0$ (left), $J = 0.24$ (middle), and $J = 0.6$ (right).

d) $J = 0.6$ ($V_\infty = 12$ m/s) are shown in Fig. 8. Beside the pronounced radial flow, the oil-flow patterns clearly reveal the presence of a laminar separation bubble for the cases of $J = 0$, 0.24, and 0.4. The thickness of the oil is larger in portions of the blade surface where the chordwise pressure gradient is almost zero, that is, in LSB and regions where the flow is simply separated, as at the root. The chordwise size of the LSB is determined from the distance between the laminar separation and reattachment lines, indicated in the figure with S and R, respectively. As the advance ratio increases from 0 to 0.4, the angle of attack over the entire blade decreases, and the LSB is expected to increase in length and move toward the trailing edge. This trend has been observed for steady airfoils from several authors [8,10]. For finite wing, the similarity with airfoils in LSB topology is restricted to inboard regions with weakly three-dimensional flow [30]. Near the tip, the wingtip vortex reduces the effective angle of attack, and the LSB is delayed and enlarged [11,31]. Moreover, the LSB is washed out in the tip region wet by the wingtip vortex.

At $J = 0$ the LSB is not present at the tip region, and, as the outboard region is approached, the LSB has a curved separation line, that is, it shortens and moves closer to the leading edge. The first phenomenon is hypothesized to be caused by the blade vortex interaction, that washes out the LSB at the tip. The curved separation line is also ascribed to a tip vortex effect; in fact, as soon as the vortex is released, it is convected mostly inward (following the streamtube), as shown in a complementary work from the authors about the same propeller [32]. This creates upwash on the blade outboard regions with a consequent increase of the angle of attack. The local change of α could explain the movement and shortening of the LSB. As J increases, the tip vortex loses strength and is convected downstream with higher velocity. This could be the reason why the tip vortex does not seem to have any influence for the cases $J = 0.24$ and 0.4, showing an LSB that extends up to the tip. From a qualitative observation, the length of the LSB increases in the spanwise direction (from the root to the tip) due to the decrease of α. Furthermore, the case $J = 0.4$ exhibits a wider LSB with respect to $J = 0.24$ due to the lower α over the entire blade. Finally, the case $J = 0.6$ also does not manifest any tip vortex effect. Since this case corresponds with the lowest α over the blade, the separation line is delayed toward the trailing edge. It is not clear if the shear layer reattaches at the thin black region at the trailing edge or stays separated. In the latter case, it would mean that the LSB bursts at low angles of attack, as found by Park et al. [12] and Kim et al. [9]. This will be further examined in the following sections.

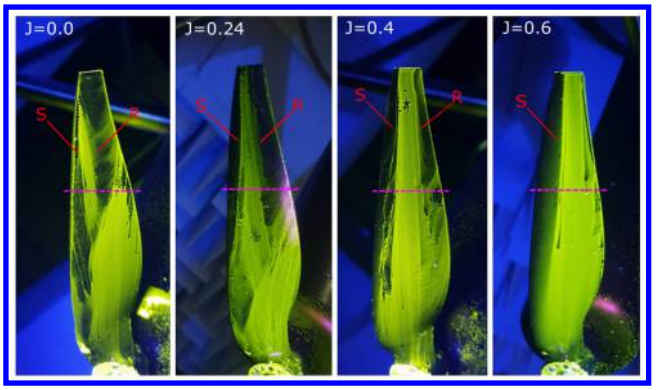

Fig. 8 Oil-flow visualizations of the suction side of the blade at 4000 rpm and $J = 0$, 0.24, 0.4, and 0.6.

The separation bubble characteristics depend also on the Reynolds number, but the dependence on the angle of attack is stronger. In the present study, when the advance ratio increases from 0 to 0.6, the corresponding chord-based Reynolds number increase is 3.7×10^3, and it is considered negligible.

B. Aerodynamic Performance

Figure 9 shows the experimental thrust and torque coefficients and the propulsive efficiency as a function of the advance ratio J. The parabolic relation between thrust coefficient and advance ratio for small-scale propellers has been found also from other authors [33,34]. The torque coefficient exhibits an almost constant part between $J = 0$ and 0.4. At this regime, the sections of the blade closer to the root that are separated contribute to most of the torque with high drag values. As the advance ratio increases, the blades section angle of attack reduces below the stall angle, and the torque decreases as a consequence of less drag. The propulsive efficiency is characterized, as expected, by an opposite trend: as the torque decreases, the propulsive efficiency increases [see Eq. (1)]. The maximum is equal to $\eta_{\text{prop}} = 0.78$ at $J = 0.6$.

C. Mean and RMS Velocity Fields

Figure 10 shows the distribution of dimensionless relative velocity and rms velocity around the cross section at 60% of the blade radius (highlighted by the dashed line in Fig. 8). The black region constitutes the airfoil surface, while the white parts adjacent to the surface represent regions where the velocity vectors are corrupted due to small movements of the blade during the phase-locked measurements or to surface reflections. As expected, most of the flow acceleration occurs at the suction side of the airfoil and only partially at the pressure side. The decrease of velocity in the wake region is also well captured. As J increases, the velocity at the suction side decreases, and the stagnation point moves toward the leading edge. This corresponds to a reduction of the angle of attack, in agreement with the description in Sec. II.G. The maximum velocity reached at $J = 0$ (Fig. 10a) is equal to 1.58 times the relative freestream velocity V_{R_∞} and at $J = 0.6$ (Fig. 10d) is $1.3V_{R_\infty}$.

The rms velocity contours show a region at the suction side and in the wake of the airfoil where a considerable increase occurs. When the angle of attack decreases (J increases), the chordwise point where the rms velocity increases moves toward the trailing edge. The region where the rms velocity suddenly starts to increase may be associated with the location of boundary-layer transition onset, which is in the vicinity of the reattachment point. Due to the poor near-wall resolution, the exact location of boundary-layer transition on the airfoil

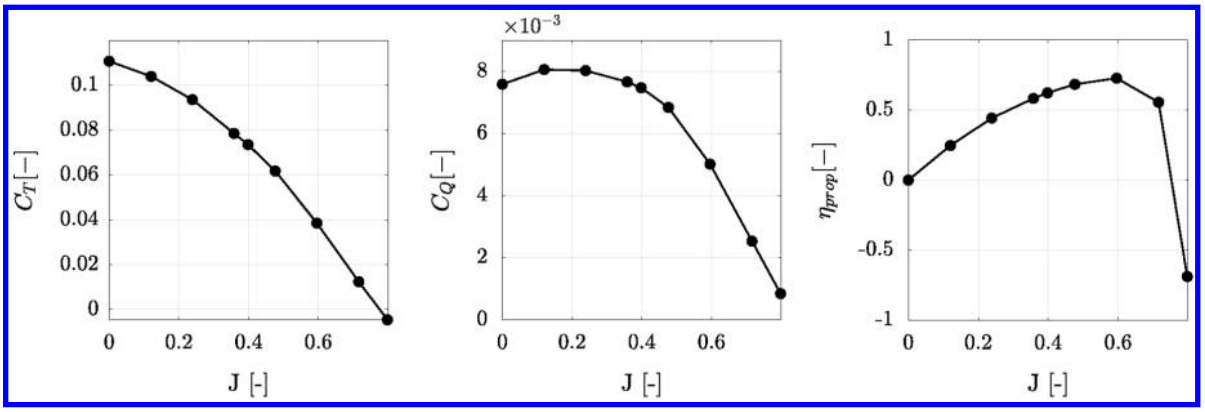

Fig. 9 Thrust coefficient (left), torque coefficient (middle), and propulsive efficiency (right) versus J at 4000 rpm.

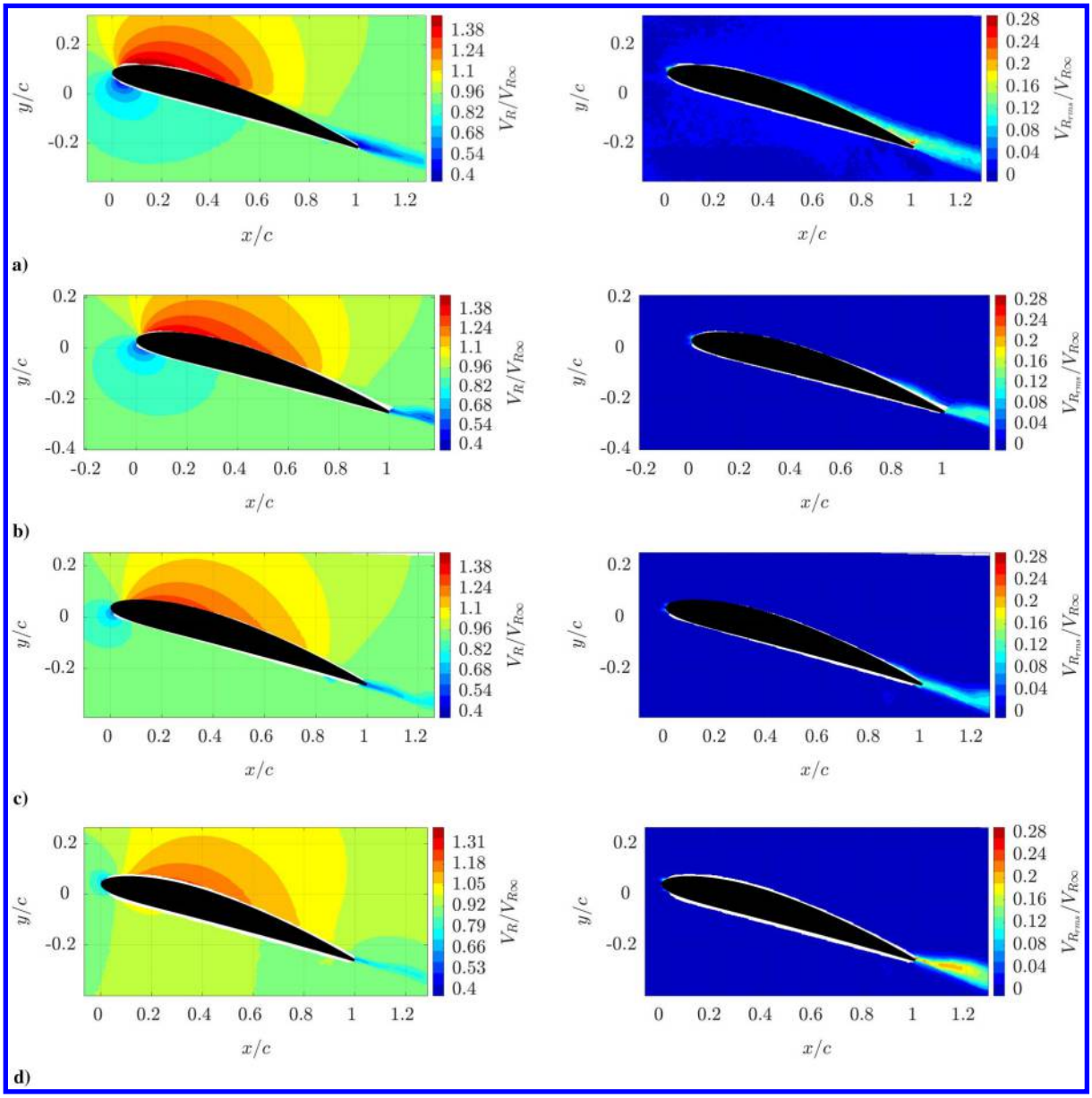

Fig. 10 Mean and rms velocity fields around the blade cross section at $r/R = 0.6$ at 4000 rpm: a) $J = 0$, b) $J = 0.24$, c) $J = 0.4$, and d)$J = 0.6$.

suction side cannot be estimated; however, the following is evident. At $J = 0$ (Fig. 10a) the rms velocity starts increasing at about $x/c = 0.4$ with values exceeding 10% of freestream velocity. The cases $J = 0.24$ (Fig. 10b) and $J = 0.4$ (Fig. 10c) present similar characteristics: the higher rms velocity values are confined in a thin region close to the trailing edge and wake, from about $x/c = 0.8$ for the first case and $x/c = 0.9$ for the second one. The values are around 12% of freestream velocity. Interestingly, the case $J = 0.6$ (Fig. 10d) exhibits an rms velocity amplification only in the wake, with values reaching 22% of freestream velocity. This strengthens the idea of

separation without reattachment for the case $J = 0.6$, as conjectured from the oil-flow results. The turbulent flow in the wake is in part associated with amplified unstable waves originated in the separated shear layer, which ultimately transforms in wake vortex shedding [35]. Figure 11 shows the instantaneous spanwise vorticity component around the trailing edge and wake for the cases $J = 0.4$ and 0.6. A coherent structure can be clearly identified in the wake region for both cases. At $J = 0.6$ the length scale of the vortices is approximately doubled. Indeed, when the flow fails to reattach, as at $J = 0.6$, the vortex structures increase in length, as observed by Yarusevich et al. [13] and this would explain the wider wake with higher velocity fluctuations with respect to the other cases.

D. Pressure Fields

The pressure fields have also been computed from the integration of the PIV velocity fields, by using the method described in II.E. Figures 12a, 12c, 12e, and 12g display the pressure coefficient C_p distributions around the blade section, respectively, at $J = 0$, $J = 0.24$, $J = 0.4$, and $J = 0.6$. The results are consistent with the velocity distributions; in fact, the intensity of the suction peak is increasing as the advance ratio increases. The minimum C_p is equal to -1.2 for the case $J = 0$ and -0.6 for $J = 0.6$. The pressure coefficient at the pressure side of the airfoil is almost constant, except for the region close to the leading edge.

For each of the four cases, the C_p has been also extrapolated on the blade surface and plotted in Figs. 12b, 12d, 12f, and 12h; furthermore, comparisons with computations made via Xfoil [36] and the aerodynamic solver implemented inside *Optyδ*B-BEMT tool are included. *Optyδ*B-BEMT is a code for the prediction of the propeller performance based on a blade element momentum theory (BEMT) developed by the authors [32]. The BEMT aerodynamic solver is based on a boundary-layer model by Drela and Giles [37] coupled with a second-order panel method through an iterative process based on the boundary-layer transpiration velocity. A pressure plateau can be identified in all the four figures. As explained in Sec. I, this is associated to regions where the boundary layer is separated. The increase of pressure after the plateau, observed for $J = 0$, 0.24, and 0.4, indicates a boundary-layer reattachment. This confirms the presence of an LSB over the blade surface, as already shown by the oil flow. The trend of the LSB with the advance ratio, which can be retrieved by the extent and position of the pressure plateau, is also in agreement with the oil-flow visualizations. As the advance ratio increases (angle of attack decreases), the region of nearly constant pressure becomes wider and moves toward the leading edge, which means that the bubble is decreasing in length and moving upstream. A similar trend of the LSB is predicted by Xfoil for these three cases, but the reattachment location is overestimated. When using *Optyδ*B-BEMT, the best match with the experimental curves has been found with an angle of attack of 1 deg smaller than Xfoil. The predicted trend is similar to Xfoil but with an earlier transition location and a better match at $J = 0$. The case $J = 0.6$ (Fig. 12f) exhibits a region of nearly constant pressure that extends up to the trailing edge. This supports the theory that the flow is separated up to the trailing edge. For this case Xfoil and *Optyδ*B-BEMT predict a long LSB with the reattachment point at $x/c = 0.9$ and 0.7, respectively.

E. Far-Field Noise

A comparison of noise spectra at a fixed rpm of 4000, by varying the advance ratio J from 0 to 0.6 is presented in Fig. 13. The spectra are computed using the pressure signals from microphones 3 (above the rotor plane), 7 (at the rotor plane), and 11 (below the rotor plane) of the array (see Fig. 3). All the microphone spectra present both discrete tones, mostly occurring at multiples of the BPF, and a broadband contribution. The most significant sources of broadband noise are: turbulent boundary-layer trailing-edge noise and turbulence ingestion noise at the leading edge. An additional near-wake source is due to the vortex shedding originated from the laminar separation region.

For all the cases the trailing-edge noise is mainly responsible for the broadband noise at low-to-mid frequency range, up to about BPF 20 (2.7 KHz). The small decrease of broadband noise in this frequency range when J switches from 0 to 0.4 can be partially related to the variation of the integral boundary-layer parameters at the trailing edge, such as momentum, displacement, and total thickness, which are expected to decrease when the laminar-to-turbulent transition point moves toward the trailing edge. For the hover case $J = 0$, the broadband level is several dB higher with respect to the other advance ratios. This can be attributed not only to trailing-edge noise, but also to turbulence impingement noise at the leading edge [7]. The last condition to analyze is $J = 0.6$, corresponding with the lowest blade loading and angles of attack over the blade. In this case the broadband level is contaminated by the background noise up to BPF 1, while the small increase up to BPF 20 with respect to $J = 0.4$ is associated with a different growing trend of the boundary-layer

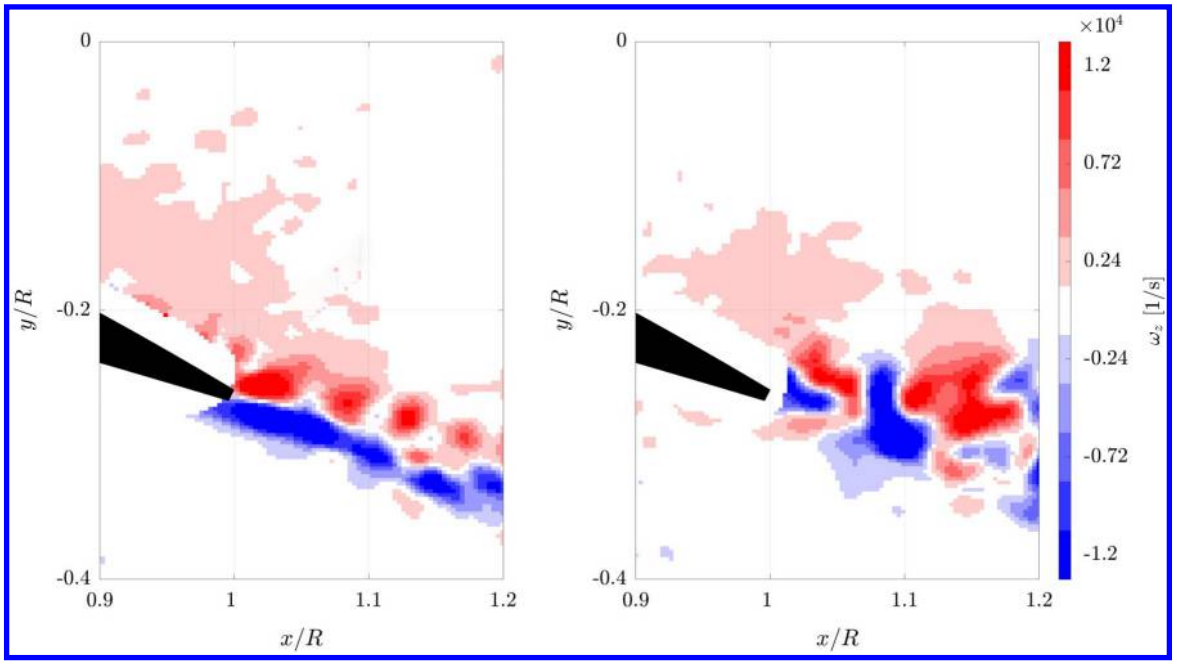

Fig. 11 Instantaneous spanwise vorticity distribution around the trailing edge and wake of the blade cross section at $r/R = 0.6$ at 4000 rpm and $J = 0.4$ (left) and $J = 0.6$ (right).

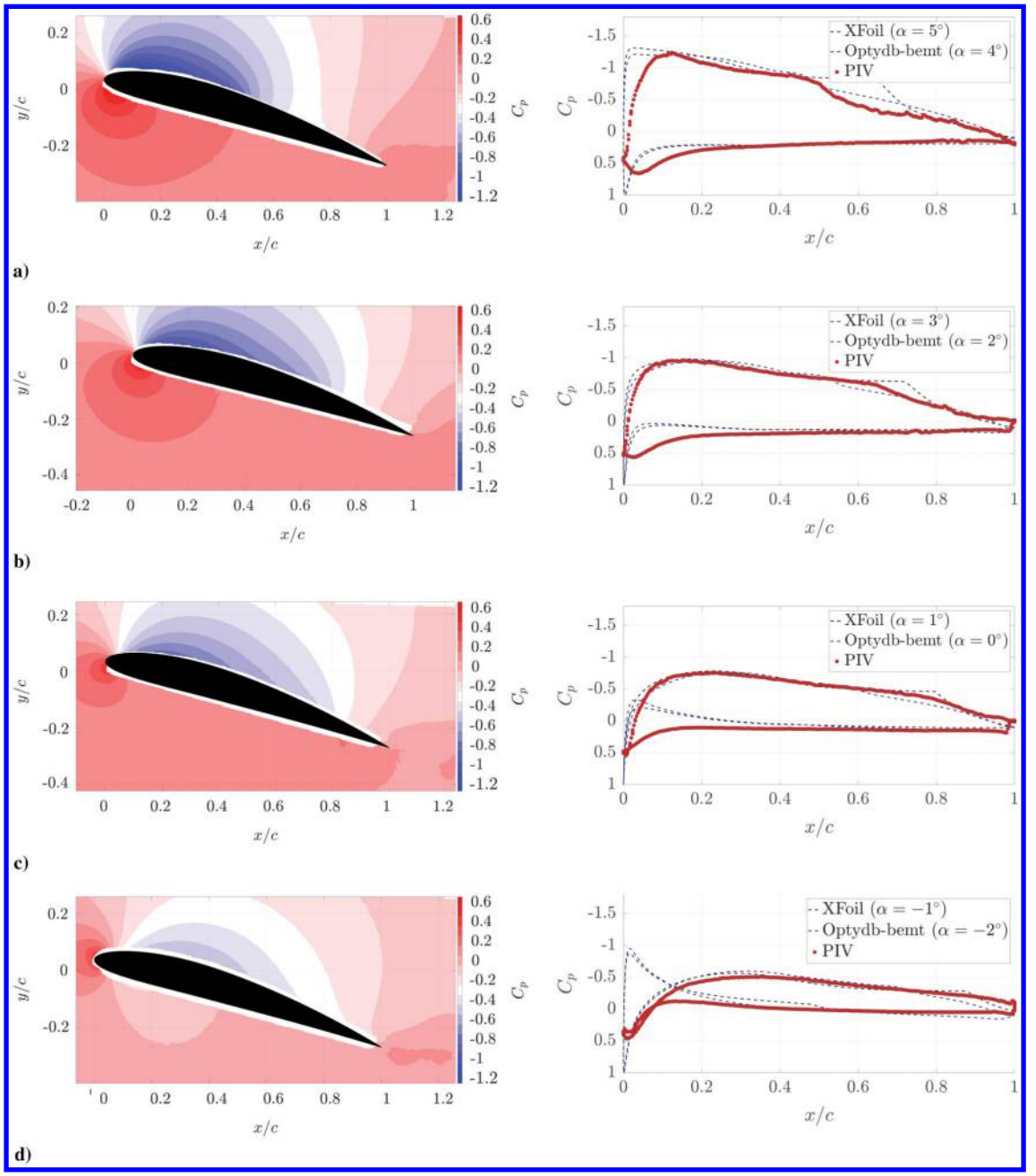

Fig. 12 Pressure coefficients around the blade cross section at $r/R = 0.6$ at 4000 rpm: a)$J = 0$, c) $J = 0.24$, e) $J = 0.4$, and g)$J = 0.6$. Each field is combined with the corresponding surface pressure distribution b), d), f), and h).

parameters due to the flow separation that extends over the entire blade span (see Fig. 8). The vortex shedding originated from the laminar separation region, which ultimately transforms into wake vortex shedding, constitutes another important source of noise responsible for the hump at high frequency, centered at about BPF 50 (7 KHz). This frequency matches with the frequency calculated using the characteristic wavelength of the vortical structures in the wake (shown in Fig. 11) and the wake convection velocity, equal to about 0.003 m and 20 m/s, respectively. A very similar hump at the same frequency range has been found from Wu et al. [20] from a numerical simulation on an airfoil at $Re_c = 1.5 \cdot 10^5$. The hump is clearly visible at all the advance ratios, and its amplitude increases of about 10 dB when the J increases from 0 to 0.6. The more efficient noise emission as J increases is associated with an increase in length scale and coherence of the vortices when the laminar separation region become wider.

The steady pressure distribution across the rotor, associated with steady loading, is responsible for BPF 1 and 2 [38]. The amplitude of the BPF 1 decreases as the advance ratio increases. This is related to the reduction of thrust with the advance ratio (see Fig. 9). At positive advance ratios, the tones at higher harmonics (BPF 5–BPF 100) are associated to the motor electrical noise, as shown in the preceding section. The appearance of tones in hover conditions $J = 0$ can be associated with unsteady pressure fluctuations due to blade vortex interaction, that is, the impact of a blade with the tip vortex generated by the successive blade, as shown by Gourdain et al. [39]. When the advance ratio is increased, the wake is convected downstream, and no interaction takes place. It can be noted that, in hover condition, the tones show an increasing trend up to BPF 10. Nardari et al. [40] proved that additional tonal energy in the midfrequency range is generated by unsteady blade loading due to flow recirculation in a confined environment, as in the anechoic chamber, and tones from BPF 2 to 30 for the confined condition are up to 10 dB higher with respect to the unconfined case. The BPF 1, due to steady loading, and the high-frequency part of the spectra are insensitive to flow recirculation.

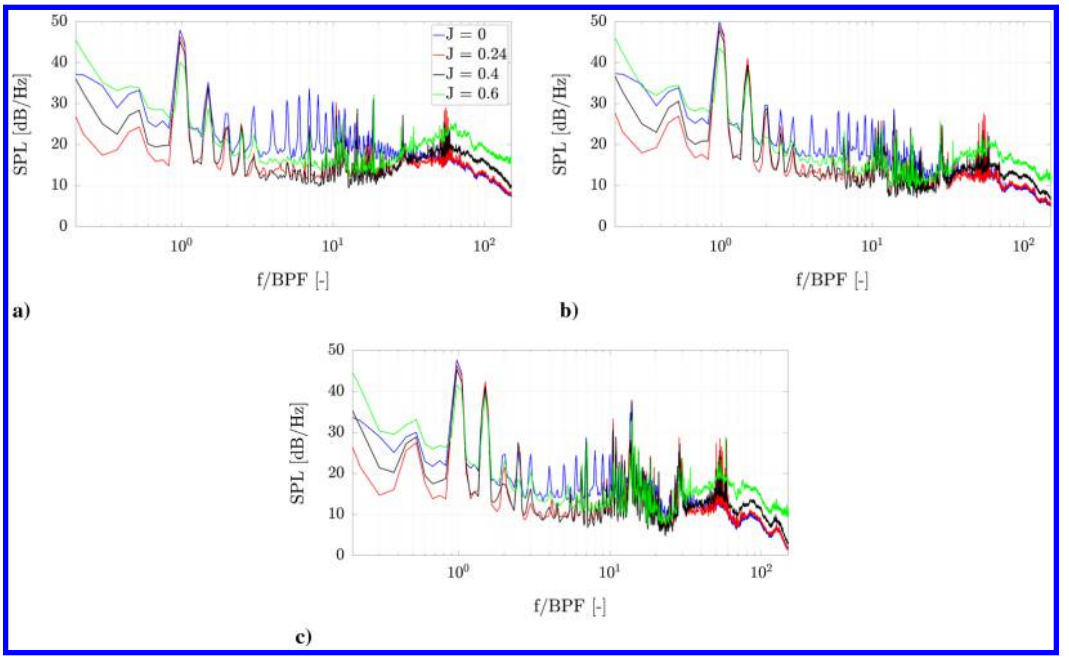

Fig. 13 Comparison of noise spectra at 4000 rpm measured with a) mic 3, b) mic 7, and c) mic 11 by varying the advance ratio J from 0 to 0.6.

V. Conclusions

A small-scale UAV propeller operating at a chord-based Reynolds number of the order of 10^4 has been studied experimentally in terms of characteristics of the flow development over the blade and the far-field noise, via oil-flow visualizations, phase-locked PIV, and microphone measurements. Insights about the boundary-layer behavior are retrieved through the analysis of mean and rms velocity, spanwise vorticity, and static pressure calculated from the PIV velocity.

The main acoustic contamination during the experimental campaign turns out to be the motor noise that is responsible for a series of discrete tones at mid-to-high frequency range (BPF 5–BPF 100). The maximum uncertainty of the main tone level is related to the instantaneous variation of the propeller rotational speed, and it is shown to be about 2 dB.

The oil-flow and PIV results reveal the presence of a laminar separation bubble (LSB) on the suction side of the blade for $J = 0, 0.24$, and 0.4. The LSB is found to move toward the leading edge and decreases in size when the angle of attack is increased, or rather, the advance ratio J is decreased. As far as the authors' knowledge, it is the first time that an LSB has been visualized on such a small-scale propeller. The case $J = 0$ is the only one where the LSB does not extend up to the very tip region. The hypothesis is that the blade vortex interaction washes out the LSB at the tip. The case $J = 0.6$ shows a long bubble without clear evidence of reattachment. The more pronounced velocity fluctuations in the wake with respect to the other cases are mainly associated with a wake vortex shedding that is more efficient at $J = 0.6$, due to coherent structure with a bigger length scale. Noise spectra in hover condition exhibit a stronger tonal contribution, as a result of unsteady loading, with respect to cases at positive advance ratios. The main broadband noise sources at low-to-mid frequency range associated with the different advance ratio conditions are different. For the case $J = 0$, turbulence ingestion noise at the leading edge is believed to be the dominant source. The turbulence impinging the leading edge is generated by the wake of the previous blade. At $J = 0.24$, 0.4, and 0.6, the trailing-edge noise source is expected to become the dominant one. The small differences in the noise levels are associated with different trends of the boundary-layer integral parameters at the trailing edge, in turn related with different positions of the laminar-to-turbulent transition and reattachment points. The high frequency hump, visible for all the cases, is caused by the wake vortex shedding, originated from the laminar separation region. The bigger dimension of the vortices at $J = 0.6$ makes the noise emission at high-frequency 10 dB more efficient with respect to the case $J = 0$.

References

[1] Casalino, D., van der Velden, W., Romani, G., and Gonzalez-Martino, I., "Aeroacoustic Analysis of Urban Air Operations Using the LB/VLES Method," *25th AIAA/CEAS Aeroacoustics Conference*, AIAA Paper 2019-2662, 2019. https://doi.org/10.2514/6.2019-2662

[2] Casalino, D., van der Velden, W., and Romani, G., "Community Noise of Urban Air Transportation Vehicles," *2019 AIAA Aerospace Sciences Meeting*, AIAA Paper 2019-1834, 2019. https://doi.org/10.2514/6.2019-1834

[3] Winslow, J., Otsuka, H., Govindarajan, B., and Chopra, I., "Basic Understanding of Airfoil Characteristics at Low Reynolds Numbers (104-105)," *Journal of Aircraft*, Vol. 55, No. 3, 2017, pp. 1–0. https://doi.org/10.2514/1.C034415

[4] Genç, M., Koca, K., Açkel, H., Özkan, G., Kırış, M., and Yıldız, R., "Flow Characteristics over NACA4412 Airfoil at Low Reynolds Number," *European Physical Journal Conferences*, Vol. 114, March 2016, Paper 02029. https://doi.org/10.1051/epjconf/201611402029

[5] Sunada, S., Ozaki, K., Tanaka, M., Yasuda, T., Yasuda, K., and Kawachi, K., "Airfoil Characteristics at a Low Reynolds Number," *Journal of Flow Visualization and Image Processing*, Vol. 7, No. 3, 2000, p. 10. https://doi.org/10.1615/JFlowVisImageProc.v7.i3.20

[6] Lin, J., and Pauley, L., "Low-Reynolds-Number Separation on an Airfoil," *AIAA Journal*, Vol. 34, No. 8, 1996, pp. 1570–1577. https://doi.org/10.2514/3.13273

[7] Serre, R., Gourdain, N., Jardin, T., López, A., Balaramraja, V., Belliot, S., Jacob, M., Moschetta, J.-M., and Maui, H., "Aerodynamic and Acoustic Analysis of an Optimized Low Reynolds Number Rotor," *Internation Symposium on Transport Phenomena and Dynamics of Rotating Machinery (ISROMAC)*, 2017.

[8] Brendel, M., and Mueller, T., "Boundary-Layer Measurements on an Airfoil at Low Reynolds Numbers," *Journal of Aircraft*, Vol. 25, No. 7, 1988, pp. 612–617. https://doi.org/10.2514/3.45631

[9] Kim, D.-H., Yang, J.-H., Chang, J.-W., and Chung, J., "Boundary Layer and Near-Wake Measurements of NACA 0012 Airfoil at Low Reynolds Numbers," AIAA Paper 2009-1472, 2009. https://doi.org/10.2514/6.2009-1472

[10] Boutilier, M., and Yarusevych, S., "Parametric Study of Separation and Transition Characteristics over an Airfoil at Low Reynolds Numbers," *Experiments in Fluids*, Vol. 52, No. 6, 2012, pp. 1491–1506. https://doi.org/10.1007/s00348-012-1270-z

[11] Bastedo, W. G., Jr., and Mueller, T. J., "Spanwise Variation of Laminar Separation Bubbles on Wings at Low Reynolds Number," *Journal of Aircraft*, Vol. 23, No. 9, 1986, pp. 687–694.

[12] Park, D., Shim, H., and Lee, Y., "PIV Measurement of Separation Bubble on an Airfoil at Low Reynolds Numbers," AIAA Paper 2019-3644, 2019. https://doi.org/10.2514/6.2019-3644

[13] Yarusevych, S., Sullivan, P., and Kawall, J., "Coherent Structures in an Airfoil Boundary Layer and Wake at Low Reynolds Numbers," *Physics of Fluids*, Vol. 18, No. 4, 2006, Paper 044101. https://doi.org/10.1063/1.2187069

[14] Hain, R., Kähler, C., and Radespiel, R., "Dynamics of Laminar Separation Bubbles at Low-Reynolds-Number Aerofoils," *Journal of Fluid Mechanics*, Vol. 630, July 2009, pp. 129–153. https://doi.org/10.1017/S0022112009006661

[15] Burgmann, S., Brücker, C., and Schröder, W., "Scanning PIV Measurements of a Laminar Separation Bubble," *Experiments in Fluids*, Vol. 41, No. 2, 2006, pp. 319–326. https://doi.org/10.1007/s00348-006-0153-6

[16] Sinibaldi, G., and Marino, L., "Experimental Analysis on the Noise of Propellers for Small UAV," *Applied Acoustics*, Vol. 74, No. 1, 2013, pp. 79–88. https://doi.org/10.1016/j.apacoust.2012.06.011

[17] Pagliaroli, T., Moschetta, J.-M., Benard, E., and Nana, C., "Noise Signature of a MAV Rotor in Hover," *3AF 49th International Symposium of Applied Aerodynamics*, 2014.

[18] Marte, J., and Kurtze, D. W., "A Review of Aerodynamic Noise From Propellers, Rotors, and Lift Fans," California Inst. of Technology TR 32-1462, Pasadena, CA, 1970.

[19] Pröbsting, S., and Yarusevych, S., "Laminar Separation Bubble Development on an Airfoil Emitting Tonal Noise," *Journal of Fluid Mechanics*, Vol. 780, Oct. 2015, pp. 167–191. https://doi.org/10.1017/jfm.2015.427

[20] Wu, H., Sanjosé, M., Moreau, S., and Sandberg, R., "Direct Numerical Simulation of the Self-Noise Radiated by the Installed Controlled-Diffusion Airfoil at Transitional Reynolds Number," AIAA Paper 2018-3797, 2018. https://doi.org/10.2514/6.2018-3797

[21] Yang, Y., Wang, Y., Liu, Y., Hu, H., and Li, Z., "Noise Reduction and Aerodynamics of Isolated Multi-Copter Rotors with Serrated Trailing Edges During Forward Flight," *Journal of Sound and Vibration*, Vol. 489, Dec. 2020, Paper 115688.

[22] Lee, H. M., Lu, Z., Lim, K. M., Xie, J., and Lee, H. P., "Quieter Propeller with Serrated Trailing Edge," *Applied Acoustics*, Vol. 146, March 2019, pp. 227–236.

[23] Merino-Martinez, R., Rubio Carpio, A., Lima Pereira, L., Herk, S., Avallone, F., Ragni, D., and Kotsonis, M., "Aeroacoustic Design and Characterization of the 3D-Printed, Open-Jet, Anechoic Wind Tunnel of Delft University of Technology," *Applied Acoustics*, Vol. 170, Dec. 2020, Paper 107504. https://doi.org/10.1016/j.apacoust.2020.107504

[24] Scarano, F., and Riethmuller, M., "Advances in Iterative Multigrid PIV Image Processing," *Experiments in Fluids*, Vol. 29, No. 1, 2012, pp. S051–S060. https://doi.org/10.1007/s003480070007

[25] Ragni, D., Oudheusden, B., and Scarano, F., "Non-Intrusive Aerodynamic Loads Analysis of an Aircraft Propeller Blade," *Experiments in Fluids*, Vol. 51, No. 2, 2011, pp. 361–371. https://doi.org/10.1007/s00348-011-1057-7

[26] Oudheusden, B., "PIV-Based Pressure Measurement," *Measurement Science and Technology*, Vol. 24, No. 3, 2013, Paper 032001. https://doi.org/10.1088/0957-0233/24/3/032001

[27] Willert, C., "Stereoscopic Digital Particle Image Velocimetry for Application in Wind Tunnel Flows," *Measurement Science and Technology*, Vol. 8, No. 12, 1997, p. 1465.

[28] Westerweel, J., "Fundamentals of Digital Particle Image Velocimetry," *Measurement Science and Technology*, Vol. 8, No. 12, 1997, p. 1379.

[29] Schrijer, F., and Scarano, F., "Effect of Predictor–Corrector Filtering on the Stability and Spatial Resolution of Iterative PIV Interrogation," *Experiments in Fluids*, Vol. 45, No. 5, 2008, pp. 927–941.

[30] Toppings, C. E., Kurelek, J. W., and Yarusevych, S., "Laminar Separation Bubble Development on a Finite Wing," *AIAA Journal*, Vol. 59, No. 8, 2021, pp. 1–13.

[31] Genç, M. S., Özkan, G., Özden, M., Kırış, M. S., and Yıldız, R., "Interaction of Tip Vortex and Laminar Separation Bubble over Wings with Different Aspect Ratios Under Low Reynolds Numbers," *Proceedings of the Institution of Mechanical Engineers, Part C: Journal of Mechanical Engineering Science*, Vol. 232, No. 22, SAGE Publications, Thousand Oaks, CA, 2018, pp. 4019–4037.

[32] Casalino, D., Grande, E., Romani, G., Ragni, D., and Avallone, F., "Definition of a Benchmark for Low Reynolds Number Propeller Aeroacoustics," *Aerospace Science and Technology*, Vol. 113, June 2021, Paper 106707.

[33] Macneill, R., and Verstraete, D., "Blade Element Momentum Theory Extended to Model Low Reynolds Number Propeller Performance," *Aeronautical Journal*, Vol. 121, No. 1240, 2017, pp. 1–23. https://doi.org/10.1017/aer.2017.32

[34] Brandt, J., and Selig, M., "Propeller Performance Data at Low Reynolds Numbers," AIAA Paper 2011-1255, 2011. https://doi.org/10.2514/6.2011-1255

[35] Pröbsting, S., Scarano, F., and Morris, S., "Regimes of Tonal Noise on an Airfoil at Moderate Reynolds Number," *Journal of Fluid Mechanics*, Vol. 780, Oct. 2015, pp. 407–438.

[36] Drela, M., "XFOIL: An Analysis and Design System for Low Reynolds Number Airfoils," *Low Reynolds Number Aerodynamics*, edited by T. J. Mueller, Lecture Notes in Engineering, Vol. 54, Springer, Berlin, Heidelberg, 1989.

[37] Drela, M., and Giles, M., "Viscous-Inviscid Analysis of Transonic and Low Reynolds Number Airfoils," *AIAA Journal*, Vol. 25, No. 10, 1987, pp. 1347–1355. https://doi.org/10.2514/3.9789

[38] Kim, D., Park, C., and Moon, Y., "Aerodynamic Analyses on the Steady and Unsteady Loading-Noise Sources of Drone Propellers," *International Journal of Aeronautical and Space Sciences*, Vol. 20, No. 3, 2019, pp. 611–619. https://doi.org/10.1007/s42405-019-00176-3

[39] Gourdain, N., Jardin, T., Serre, R., Prothin, S., and Moschetta, J.-M., "Application of a Lattice Boltzmann Method to Some Challenges Related to Micro-Air Vehicles," *International Journal of Micro Air Vehicles*, Vol. 10, No. 3, 2018, pp. 285–299. https://doi.org/10.1177/1756829318794174

[40] Nardari, C., Casalino, D., Polidoro, F., Coralic, V., Lew, P., and Brodie, J., "Numerical and Experimental Investigation of Flow Confinement Effects on UAV Rotor Noise," AIAA Paper 2019-2497, 2019. https://doi.org/10.2514/6.2019-2497

A. R. Jones
Associate Editor

This article has been cited by:

1. Gianluca Romani, Edoardo Grande, Francesco Avallone, Daniele Ragni, Damiano Casalino. 2022. Computational study of flow incidence effects on the aeroacoustics of low blade-tip Mach number propellers. *Aerospace Science and Technology* **120**, 107275. [Crossref]